

# NIHAO-LG: The uniqueness of Local Group dwarf galaxies

Nikhil Arora,<sup>1\*</sup> Andrea V. Macciò,<sup>2,3,4</sup> Stéphane Courteau,<sup>1</sup> Tobias Buck,<sup>5</sup>  
 Noam I. Libeskind,<sup>5,6</sup> Jenny G. Sorce,<sup>5</sup> Chris B. Brook,<sup>10,11</sup> Yehuda Hoffman<sup>9</sup>  
 Gustavo Yepes,<sup>7,8</sup> and Edoardo Carlesi<sup>9</sup>

<sup>1</sup>*Department of Physics, Engineering Physics and Astronomy, Queen's University, Kingston, ON K7L 3N6, Canada*

<sup>2</sup>*New York University Abu Dhabi, PO Box 129188, Abu Dhabi, United Arab Emirates*

<sup>3</sup>*Center for Astro, Particle and Planetary Physics (CAP<sup>3</sup>), New York University Abu Dhabi*

<sup>4</sup>*Max-Planck-Institut für Astronomie, Königstuhl 17, D-69117 Heidelberg, Germany*

<sup>5</sup>*Leibniz-Institut für Astrophysik Potsdam (AIP), An der Sternwarte 16, D-14482 Potsdam, Germany*

<sup>6</sup>*University Lyon, University Claude Bernard Lyon 1, CNRS, IP2I Lyon/IN2P3, IMR 5822, F-69622, Villeurbanne, France*

<sup>7</sup>*Departamento de Física Teórica, Módulo 8, Facultad de Ciencias, Universidad Autónoma de Madrid, 28049 Madrid, Spain*

<sup>8</sup>*Centro de Investigación Avanzada en Física Fundamental (CIAFF), Universidad Autónoma de Madrid, 28049 Madrid, Spain*

<sup>9</sup>*Racah Institute of Physics, Hebrew University, Jerusalem 91904, Israel*

<sup>10</sup>*Universidad de La Laguna. Avda. Astrofísico Fco. Sánchez, E-38200, La Laguna, Tenerife, Spain*

<sup>11</sup>*Instituto de Astrofísica de Canarias, Calle Via Láctea s/n, E-38206 La Laguna, Tenerife, Spain*

Accepted XXX. Received YYY; in original form ZZZ

## ABSTRACT

Recent observational and theoretical studies of the Local Group (LG) dwarf galaxies have highlighted their unique star formation history, stellar metallicity, gas content, and kinematics. We investigate the commonality of these tantalizing features by comparing constrained LG and field central dwarf halo simulations in the NIHAO project. For the first time, constrained LG simulations performed with NIHAO hydrodynamics which track the evolution of MW and M31 along with  $\sim 100$  dwarfs in the Local Group are presented. The total gas mass and stellar properties (velocity dispersion, evolution history, etc.) of present-day LG dwarfs are found to be similar to field systems. Overall, the simulated LG dwarfs show representative stellar properties to other dwarfs in the Universe. However, relative to fields, LG dwarfs have more cold gas in their central parts and more metal-rich gas in the halo stemming from interactions with MW/M31 and/or feedback. The larger gas metal content in LG dwarfs results in early star formation events that lead to strong feedback and subsequent quenching. We also test for the impact of metal diffusion on the chemical evolution of LG dwarfs, and find that metal diffusion does not affect the stellar or gaseous content of LG relative to field dwarfs; the largest differences are found with the gas metallicity ( $\sim 0.1$  dex). Our results show that properties from LG dwarfs may be used as general constraints for studying the overall dwarf population in the Universe, providing a powerful local laboratory for galaxy formation tests and comparisons.

**Key words:** galaxies: formation – Local Group – galaxies: evolution – galaxies: dwarf – methods: numerical

## 1 INTRODUCTION

In the  $\Lambda$ CDM paradigm, galaxy growth occurs through hierarchical assembly and secular evolution (White & Rees 1978; White & Frenk 1991; Kormendy & Sanders 1992). As a result, galaxies are dynamic entities that form and evolve within groups and clusters. This holds for our Milky Way (MW) and the Andromeda galaxy (M31), which along with

numerous dwarf galaxies, form the Local Group (LG) of galaxies (Mateo 1998; McConnachie 2012; Kirby et al. 2013).

LG dwarf galaxies offer a superb laboratory to study the physics of galaxy formation. Indeed numerous observational studies of the very nearby dwarf galaxies have been conducted. In parallel dwarf galaxies in general have been the subject of many theoretical studies, mostly by means of cosmological numerical simulations. A fundamental question than arises as to how representative are the LG dwarfs of the general dwarf galaxies population. Alternatively one can ask to what extent the study of the LG dwarfs teaches us

\* E-mail: nikhil.arora@queensu.ca

about galaxy formation at large. One might think that tidal interactions between dwarf galaxies and MW/M31 can lead to formation of streams and eventual phase mixing into the stellar halos of MW/M31. These interactions can also attract pristine gas that may induce star formation and evolution of metals in dwarf galaxies (Buck 2020). Such interactions can also lead to the stripping of gas leading to a “freeze out” of the stellar population in LG dwarfs. Can such environmental interactions distinguish the LG dwarfs from the general population of dwarfs in the Universe? What are the cosmological ramifications of such difference? This Copernican question is the main motivation that leads to the present paper.

The stellar assembly of dwarf galaxies in the LG is sensitive to internal (feedback and winds) and environmental (ram pressure and tidal stripping) processes, as well as the reionization of gas due to the UV background at early times. As a result, the star formation histories (SFH) for many LG dwarfs have been extensively studied to better understand the influence of these internal and external processes. Some of these dwarfs form a large fraction of their stars at early times and are quenched after reionization (Sand et al. 2010; Brown et al. 2012; Okamoto et al. 2012) while others show moderate and continuous star formation to present day (Weisz et al. 2014; Gallart et al. 2015). Overall, SFHs of dwarfs are the product of reionization and the environment in which they formed. Gallart et al. (2015) have also shown that dwarfs with no current star formation could form in dense, cluster/group-like environments. Dwarfs that form in low density environment could retain their gas reservoir for continuous star formation and a younger stellar populations.

The presence of MW/M31 is likely to influence the gas, and therefore the stellar, content of LG dwarfs. Indeed, the fraction of neutral hydrogen in LG dwarf galaxies increases with distance from the MW (Spekkens et al. 2014; Putman et al. 2021). Dwarfs within the virial radius of the MW are especially deficient in cold gas while those outside the virial radius abound in neutral gas, almost by a factor 100 (Einasto et al. 1974; Grcevich & Putman 2009; McConnachie 2012; Spekkens et al. 2014). Gas poor systems result largely from interactions with the hot halo of the MW typically characterized by ram pressure stripping, viscous stripping, and starvation (Gunn & Gott 1972; Hester 2006; Kawata & Mulchaey 2008; Fillingham et al. 2016).

While the evolution of dwarf galaxies seems broadly understood, the key question remains: are the observed features of LG dwarfs unique or do field dwarfs, with no massive companion, show similar evolutionary tracks? A robust answer to this question must rest on two pillars. One is our ability to simulate the formation of the LG and its nearby neighborhood in way that reproduces the main features of the LG. Namely, simulations that are constrained to emulate the formation and evolution of the LG dwarfs within the ‘context’ of the actual observed LG. The other pillar consists of a detailed census of LG and field dwarfs in the Local Universe. Depending on the choice of Stellar Mass - Halo Mass relation (SHMR), especially for the low mass end, about 0.3-0.4  $\text{deg}^{-2}$  of field dwarfs with surface brightness of  $\sim 30 \text{ mag arcsec}^{-2}$  are expected in the Local Volume, with distances between 3 and 10 Mpc from us (Danieli et al. 2018). Until the advent of deep large sky surveys, such as those provided by the Rubin Observatory with a limiting magnitude of 32 mag

$\text{arcsec}^{-2}$ , comparisons with complete census of field dwarfs is beyond reach. While, the presence (or the lack) of unique aspects of the LG cannot currently be characterized with observed galaxies, high resolution simulations may provide much valuable insight.

Identifying differences between LG and field dwarf galaxies can help in better isolating the role of environment in shaping the galaxy properties in the Local Universe. In the context of other groups and cluster, galaxy properties like mean stellar age (Thomas et al. 2005; Clemens et al. 2006), morphology (Blanton & Moustakas 2009, and references therein), colour (Wilman et al. 2010; Cluver et al. 2020) and star formation rates (Fossati et al. 2015) have been shown to be strongly dependent on environment. Similar conclusions have been drawn about the influence of MW/M31 on LG dwarfs (e.g., Gottloeber et al. 2010; Benítez-Llambay et al. 2015, 2016; Buck et al. 2019; Genina et al. 2019; Libeskind et al. 2020; Di Cintio et al. 2021). However, if there exist no differences between LG and field dwarf, the nearby dwarf population (which are more easily accessible) can be used to study systems further away.

This paper presents such a comparison between the dwarf populations found in the LG and in the field through high-resolution simulations in order to highlight any similarities and differences. To this end, we take advantage of the NIHAO simulations which trace the evolution of individual dark matter halos and its baryonic components for the complete history of the Universe (Wang et al. 2015). The NIHAO simulations have already proven to be successful in matching various observations aspects of galaxy formation and evolution (Macciò et al. 2016, 2017; Obreja et al. 2019; Buck et al. 2020; Blank et al. 2021, to name a few). More details for the simulations are provided in Sec. 2.1.

Our field dwarfs sample uses NIHAO halos as presented in Wang et al. (2015). The LG dwarf sample is comprised of two constrained LG simulations with initial conditions provided from the CLUES collaboration (Gottloeber et al. 2010), presented here for the first time, and performed with the exact same code and hydrodynamics used for the NIHAO project. The constrained LG simulation allowed for the evolution of LG environment containing the MW and M31 like halos and their associated dwarfs. Our comparisons rely mostly on well-known galaxy scaling relations such as the stellar mass–metallicity relation (hereafter MZR; Gallazzi et al. 2005; McConnachie 2012; Kirby et al. 2013), stellar mass–gas mass relation (Peeples et al. 2014), star formation main sequence (SFMS; Cluver et al. 2017), and the SHMR (Behroozi et al. 2013; Moster et al. 2014).

Because the formation and evolution of dwarfs in high-resolution simulations is sensitive to the implemented sub-grid prescriptions such as feedback, chemical enrichment and metal diffusion, we also compare the subgrid physics formalism that may drive the pre-enrichment of LG dwarfs; namely metal diffusion. The impact of metal diffusion of the stellar assembly, star formation rates and chemical evolution of dwarfs galaxies still remains unclear. For instance, while Su et al. (2017) used the FIRE (Feedback In Realistic Environment; Hopkins et al. 2018) simulations to show that the sub-grid metal diffusion does not impact star formation rates on the galactic scales, Pilkington et al. (2012) and Williamson et al. (2016) found opposite results for the abundance of low-metallicity stars in dwarf galaxies (see also

Kawata et al. 2014 and Escala et al. 2018). Given the current muddled picture about the evolution and abundance of metals in LG and field dwarfs, we present results from two constrained LG simulations; with and without metal diffusion.

This paper is organised as follows: Sec. 2 outlines the NIHAO galaxy simulation which provides the field galaxy sample for this study. The two constrained Local Group simulations are also presented in Sec. 2. Sec. 3 highlights the similarities and differences between the constrained LG dwarf galaxies and the NIHAO dwarf galaxies at  $z \sim 0$ . A multi-faceted analysis of the dwarf galaxies using various galaxy scaling relations is also presented. The evolution of galaxy properties in all three simulations to better understand the difference seen at  $z = 0$  between the LG and the field is addressed in Sec. 4, and conclusions are presented in Sec. 5 as we ponder the uniqueness (or lack thereof) of LG dwarfs and its implications.

## 2 SIMULATIONS

### 2.1 NIHAO Galaxy Simulations

Our field central galaxy sample relies on the ‘‘Numerical Investigation of a Hundred Astrophysical Objects’’ (NIHAO) cosmological zoom-in simulations presented in Wang et al. (2015). The simulations were run with a flat  $\Lambda$ CDM cosmology with parameters from the *Planck satellite*:  $H_0 = 100h \text{ km s}^{-1} \text{ Mpc}^{-1}$  with  $h = 0.671$ ,  $\Omega_m = 0.3175$ ,  $\Omega_\Lambda = 0.6824$ ,  $\Omega_b = 0.049$ ,  $\sigma_8 = 0.8344$  and  $n = 0.9624$  (Planck Collaboration et al. 2014). The hydrodynamics were performed with the updated N-body SPH solver GASOLINE2 (Wadsley et al. 2017) which includes the treatment of  $P/\rho^2$  proposed by Ritchie & Thomas (2001). Gas cooling was performed through hydrogen, helium and various metal-lines in a uniform UV ionizing background. Photo-ionization and heating of the gas also occur via UV background and Compton cooling with temperatures from 10 to  $10^9$  K (Shen et al. 2010).

All NIHAO galaxies were allowed to form stars provided that the gas follows the Kennicutt-Schmidt law (Kennicutt 1998) with suitable density and temperature thresholds,  $T < 15000 \text{ K}$  and  $n_{\text{th}} > 10.3 \text{ cm}^{-3}$ . Energy is re-injected back into the interstellar medium (ISM) from stars through stellar and blast wave supernova feedback. Massive stars also ionize the ISM prior to their supernova explosion; this is referred to as ‘‘early stellar feedback’’ (Stinson et al. 2006; Wang et al. 2015) where 13% of the total stellar flux of  $2 \times 10^{50} \text{ erg M}_\odot^{-1}$  is injected into the ISM. This differs from the original prescription presented in Stinson et al. (2013) in order to account for the increased mixing of gas and aligns with the abundance matching results on MW scale presented in Behroozi et al. (2013). For supernova feedback, massive stars with  $8 M_\odot < M_* < 40 M_\odot$  inject energy of  $10^{51} \text{ erg}$  and metals into the the ISM. Because the energy is injected into high density gas, it radiates away via efficient cooling on short timescales. Therefore, for gas particles inside the blast radius, cooling is delayed by 30 Myr (Stinson et al. 2013) to prevent immediate radiation from high density gas particles (Stinson et al. 2006). The spiral and dwarf galaxies generated by NIHAO simulations have been shown to

match numerous observed galaxy properties and scaling relations (Macciò et al. 2016; Obreja et al. 2016; Buck et al. 2017; Dutton et al. 2017). The NIHAO galaxy simulations result in numerically converged galaxies as shown by the ultra high-definition NIHAO runs Buck et al. (2020).

### 2.2 NIHAO Local Group Simulations

Our sample of dwarf galaxies in a LG environment was created with initial conditions from the Constrained Local UniversE Simulations (CLUES) project<sup>1</sup> (Gottloeber et al. 2010; Carlesi et al. 2016; Sorce et al. 2016; Libeskind et al. 2020). Constrained simulations allowed us to track the position and environment of the MW, M31 like-galaxies and their associated dwarfs. The halos were identified and tracked in a cosmological box of  $100 \text{ Mpc h}^{-1}$  on a side, and constrained by observational data of the nearby Universe. The initial conditions for the simulation box relied on the Weiner filter (WF; Hoffman & Ribak 1991; Hoffman 2009), a Bayesian linear algorithm, and constrained realizations of the Gaussian matter density field from observations of the Local Universe and an assumed prior model (Zaroubi et al. 1995). The WF filter allowed for the construction of the cosmic displacement field needed to robustly model particle positions as a function of time for the constrained objects. The cosmic displacement field was created via a peculiar velocity field of the Local Universe using the CosmicFlows-2 (CF2) catalogue of galaxy redshift and direct distances (Tully et al. 2013). Malmquist biases and lognormal errors in the CF2 dataset are corrected using the bias minimization technique described in Sorce (2015). To correct for such displacements due to cosmic evolution, to calculate the positions of the galaxies progenitors, the reverse Zel’dovich approximation was applied (Doumler et al. 2013; Sorce et al. 2014). Finally, re-normalization of the velocity field is performed to get particles with initial velocity values of the particles in the simulation box. A more detailed description of the CLUES initial conditions is found in Carlesi et al. (2016); Sorce & Guo (2016); Sorce (2018); Libeskind et al. (2020).

The initial conditions from CLUES simulations with the cosmology of NIHAO and hydrodynamics from ESF-GASOLINE2 lead to the constrained NIHAO-LG simulations. Along with the effect of environment (field vs. LG), we also monitored the variations in galaxy properties due to changes in subgrid physics implementations; esp. the chemical evolution in dwarfs. To that end, we created two sets of constrained LG simulations; (i) NIHAO-LG: full NIHAO cosmology and hydrodynamics included along with metal diffusion from Wadsley et al. (2008), and (ii) NIHAO-LG(nmd): full NIHAO cosmology and hydrodynamics with no metal diffusion. We use the Chabrier Initial Mass Function (IMF; Chabrier 2003) for stellar sampling in the simulation. As we seek differences between field central dwarfs and LG dwarfs, the variation of chemical evolution is an obvious implementation to modulate. In Tab. 1, we summarize basic properties of the three NIHAO simulations used in this study. Within our constrained LG simulations, two massive halos are found with total mass  $M_{200} \sim 10^{12} M_\odot$ , a ratio of stellar masses

<sup>1</sup> <http://www.clues-project.org>.

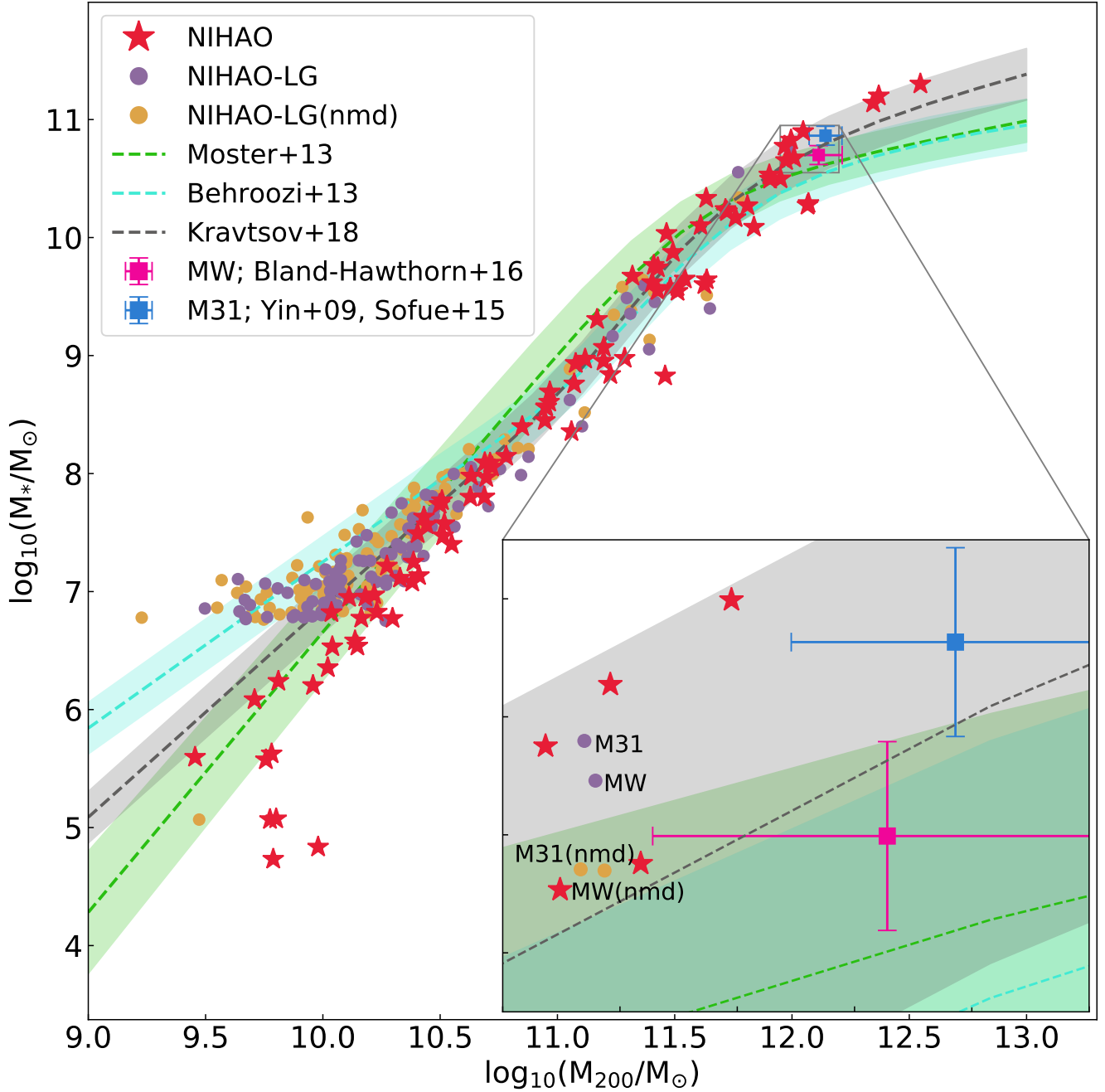


**Figure 1.** Stellar mass versus halo mass relation at redshift  $z = 0$  for NIHAO (red stars) and two constrained LG simulations with (purple circles) and without (gold circles) metal diffusion. The dashed lines and shaded regions depict popular abundance matching relations from [Moster et al. \(2014\)](#), [Behroozi et al. \(2013\)](#) and [Kravtsov et al. \(2018\)](#). The zoomed inset panel show MW and M31 analogues and comparisons with massive NIHAO spirals. The observed stellar and halo masses for the MW ([Bland-Hawthorn & Gerhard 2016](#)) [pink square] and M31 (stellar mass; [Yin et al. 2009](#) and halo mass; [Sofue 2015](#)) [blue square] are also presented.

Simulation	Box Size [ $\text{Mpc h}^{-1}$ ]	$m_{\text{dark}} [M_{\odot}]$	$\epsilon_{\text{dark}} [\text{pc}]$	$\epsilon_{\text{gas}} [\text{pc}]$	$N_{\text{halos}}$	$N_{\text{dwarfs}}$	Metal Diffusion?	Environment
NIHAO	60.1	$1.74 \times 10^6$	931.5	398.0	91	37	Yes	Field
NIHAO-LG	100.0	$1.62 \times 10^6$	860.3	487.7	104	64	Yes	Local Group
NIHAO-LG (nmd)	100.0	$1.62 \times 10^6$	860.3	487.7	115	73	No	Local Group

**Table 1.** Various properties of our three NIHAO simulations. Columns give the box size, mass resolution of the DM particles, softening length of the dark and gas particles, number of halos at  $z = 0$ , usage of metal diffusion, and the simulated environment.

for the massive halos of  $M_*^{\text{MW}}/M_*^{\text{M31}} \sim 1.05$ , and circular velocities of  $\sim 230 \text{ km s}^{-1}$ . The two massive halos have a virial radii of  $\sim 200 \text{ kpc}$  and are separated by  $\sim 700 \text{ kpc}$ . In both constrained LG simulations, the massive halos harbour disk stellar systems with the Virgo cluster nearby.

Unless stated otherwise, all quantities (stellar mass, cold gas mass, etc.) are measured within  $0.2R_{200}$  and dwarfs are defined as central systems at  $z = 0$  with  $7.0 \leq \log(M_*/M_\odot) \leq 9.5$ . From the constrained LG simulations, we selected all halos with 100 per cent high resolution DM particles (i.e., no pollution), having at least 1000 particles (baryon and DM) and at least 100 stellar particles. To make comparisons more robust, our study focuses on central galaxies from the LG simulations. We expect numerical resolution and convergence to only play a small role in the results presented here. The hydrodynamics, performed with GASOLINE2, as is the case for NIHAO and the constrained LG simulations, were stable with respect to convergence. Galaxy properties in the NIHAO simulations have also been shown to converge despite the varying spatial and mass resolution over a large range of halo masses. The highest resolution NIHAO dwarf galaxies presented in (Macciò et al. 2017, 2019) yielded galaxy properties in broad agreement with the general NIHAO simulated galaxy population (Wang et al. 2015).

Fig. 1 shows the stellar mass - halo mass relation (SHMR) at  $z = 0$  for the NIHAO and constrained NIHAO-LG simulations. For comparisons, the halo abundance matching relations from Moster et al. (2014), Behroozi et al. (2013) and Kravtsov et al. (2018) are also shown. The inset panel in Fig. 1 features the NIHAO field and constrained LG analogues for the MW and M31 along with observed measurements. The simulated stellar and halo masses for the MW/M31 agree with current estimates for the observed stellar and halo masses for MW (Bland-Hawthorn & Gerhard 2016) and M31 (Yin et al. 2009; Sofue 2015). As stated in Wang et al. (2015), the NIHAO galaxies, which serve as our field galaxy sample, also agree well with halo abundance matching results (Kravtsov et al. 2018). The dwarf galaxies ( $\log(M_{200}/M_\odot) \leq 10.5$ ) in the constrained LG simulations also match the abundance matching relation from Behroozi et al. (2013). Likewise, the galaxies from the constrained LG simulations with  $\log(M_{200}/M_\odot) \geq 10.5$  match the parameters of NIHAO field centrals and the SHMR of Kravtsov et al. (2018). However, dwarfs in LG simulations have stellar masses that exceed their NIHAO field counterparts by 0.2-0.3 dex, possibly indicative of additional pre-enriched gas material from the MW and M31.

The shallow potential of LG dwarf galaxies is insufficient for retaining high metallicity gas due to strong supernovae feedback and stellar winds (Dekel & Silk 1986). Therefore, excess stellar mass in the LG dwarfs, in comparison with field systems, is likely built up from high metallicity, easily cooled gas from the larger halos (MW/M31). The dwarfs in the LG may also have lower dark matter fraction for the same stellar mass in comparison with field systems as a result of interaction episodes with the massive halos (Munshi et al. 2017; Buck et al. 2019).

To further validate the NIHAO and LG simulations, we compare with observations the  $\text{sSFR}-M_*$  relation in Fig. 2. The specific star formation rate,  $\text{sSFR} = \text{SFR}/M_*$ , is the ratio of the average star formation rate (SFR) within the last 100 Myr and the enclosed stellar mass within  $0.2R_{200}$ ,  $M_*$ . In

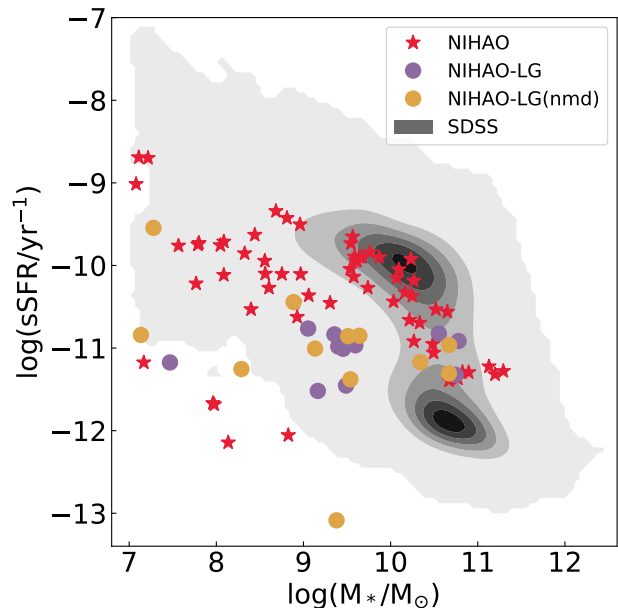


**Figure 2.** Specific star formation rate,  $\text{sSFR}(= \text{SFR}/M_*)$ , versus stellar mass,  $M_*$ , for the NIHAO (red stars) and the LG dwarf samples (purple and gold circles). The underlying grey number density distribution of SFR and  $M_*$  measurements for MPA-JHU SDSS galaxies (Kauffmann et al. 2003; Brinchmann et al. 2004) is shown for comparison.

general, both NIHAO and the constrained LG simulations match the distribution of SDSS galaxies, albeit simulated dwarfs falling in the outskirts of the observed distribution. Given the uneven selection function of the simulated NIHAO systems and the variations in measuring the observed quantities in Fig. 2, comparison of NIHAO galaxies with large-scale surveys is a non-trivial task. However, even with this complication, the overall agreement between NIHAO and the SDSS is comforting.

### 3 LOCAL GROUP GALAXIES

Our analysis begins with a variety of galaxy scaling relations at  $z = 0$ , highlighted by differences between the field and LG dwarf populations. Along with the role of environment, the impact of metal diffusion in setting some of the properties of LG dwarfs is also examined.

#### 3.1 Gas Properties

We start by comparing the gas content of dwarf galaxies in the LG and in the field. The left-hand panel of Fig. 3 shows total gas mass within  $R_{200}$  versus stellar mass (measured within  $0.2R_{200}$ ) for the field and LG dwarfs. The red line and shaded region are linear best fit and scatter for the  $M_g-M_*$  relation of the NIHAO simulation, and the data points are dwarfs from the constrained LG simulations. It is found that the overall gas content for all LG dwarfs lies within the  $1-\sigma$  scatter ( $=0.30 \pm 0.06$  dex) of the NIHAO field galaxies. A few LG dwarfs ( $\log M_* \leq 7.8$ ) deviate from the observed

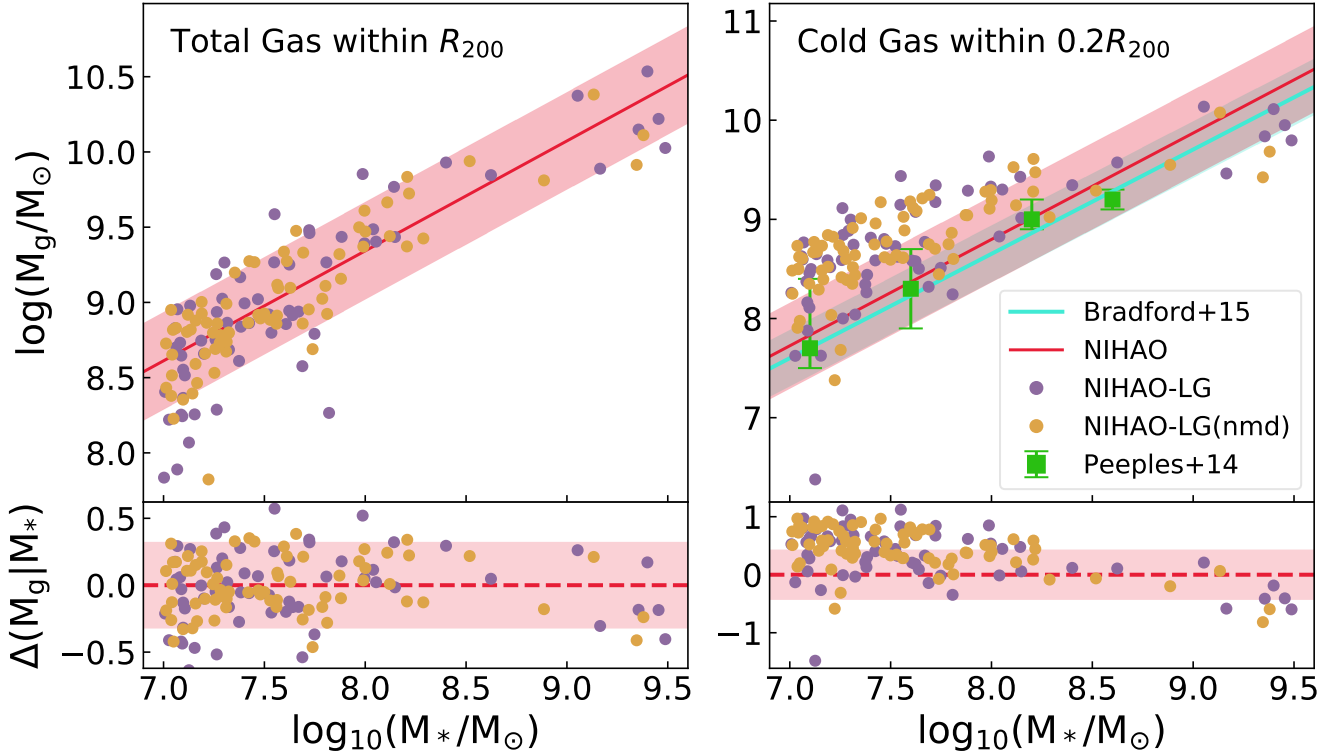


**Figure 3.** Total gas mass (left panel) and cold gas mass ( $T < 20000$  K; right panel) versus stellar mass at  $z = 0$  for the three samples of simulated dwarf galaxies. The coloured circles represent the constrained LG simulations with (purple) and without (gold) metal diffusion. The solid red line and shaded region represent a best fit for the field NIHAO dwarf galaxies and  $1-\sigma$  scatter about that fit, respectively. Total gas mass are measured within  $R_{200}$  while cold gas and stellar masses are measured within  $0.2R_{200}$ . Also shown are the cold gas - stellar mass relations from Peeples et al. (2014) and Bradford et al. (2015) in the right panel. The residuals with respect to the field dwarfs are shown in both bottom panels.

trends for field dwarf systems which might be associated to random scatter about the field galaxy relation. Most of these LG dwarfs with low gas content exhibit older, metal-poor stellar content as 50 percent of the stellar mass is formed within the first  $\sim 5$  Gyr. Stripping due to interaction with larger halos could explain the dearth of gas content in the LG dwarfs.

The right-hand panel of Fig. 3 shows the cold gas ( $T < 20000$  K) content in the field and LG dwarf systems at redshift  $z = 0$  within  $0.2R_{200}$ . This choice of radius isolates the central parts of halos as  $\sim 90\%$  of the atomic and molecular gas resides within  $0.2R_{200}$  of both the field galaxies and LG dwarfs. The  $1-\sigma$  scatter for the field dwarf relation is  $0.46 \pm 0.10$  dex or three times as large as the average residual for NIHAO-LG(nmd) of 0.14 dex. While the average residual, across the complete dwarf range, is less than the scatter for the field relation, LG dwarfs with  $\log M_* \leq 8.0$  show a larger ( $\sim 0.5$  dex) central cold gas content compared to field galaxies. While the total gas distribution for field and LG are very similar, a larger fraction of the total gas within the LG dwarfs appears to be cold gas. The residuals for the LG dwarfs with respect to the field systems, shown in the bottom right-hand panel in Fig. 3, shows a systematic trend for LG galaxies where an excess cold gas compared to fields on the low mass end and a dearth of cold gas on the high mass end.

Various observed cold gas mass - stellar mass relations from Peeples et al. (2014) and Bradford et al. (2015) are also presented in Fig. 3. The green squares represent the median cold gas mass - stellar mass relation in Peeples et al. (2014) using the observed data from McGaugh (2005, 2012), Leroy et al. (2008) and Saintonge et al. (2011). The error bars represent the 16% – 84% interquartile range of the observed data. The cyan line and shaded region, taken from Bradford et al. (2015), delineate the distribution of atomic gas mass for low mass galaxies ( $\log M_* \leq 8.6$ ) in the Sloan Digital Sky (SDSS; Aihara et al. 2011) and ALFALFA surveys (Haynes et al. 2011). While the ALFALFA survey only detects H I gas contents, the total (atomic + molecular) gas content is calculated as  $M_g = 1.4M_{H I}$ .

The cold gas content in dwarfs from both LG simulations is higher than the observed relation from Bradford et al. (2015). On the other hand, the median observed and simulated field relations show great agreement for the slopes and scatters. However, even after accounting for the atomic gas to get total gas mass, the mean observed trend shows a slightly smaller zero-point than the simulated field sample. The smaller observed gas content can be attributed to differences in how the measurements of total gas content between simulations and observations. For NIHAO, all gas particles are counted within  $0.2R_{200}$ ; however, observed measurements are limited by signal-to-noise (S/N) and the cold

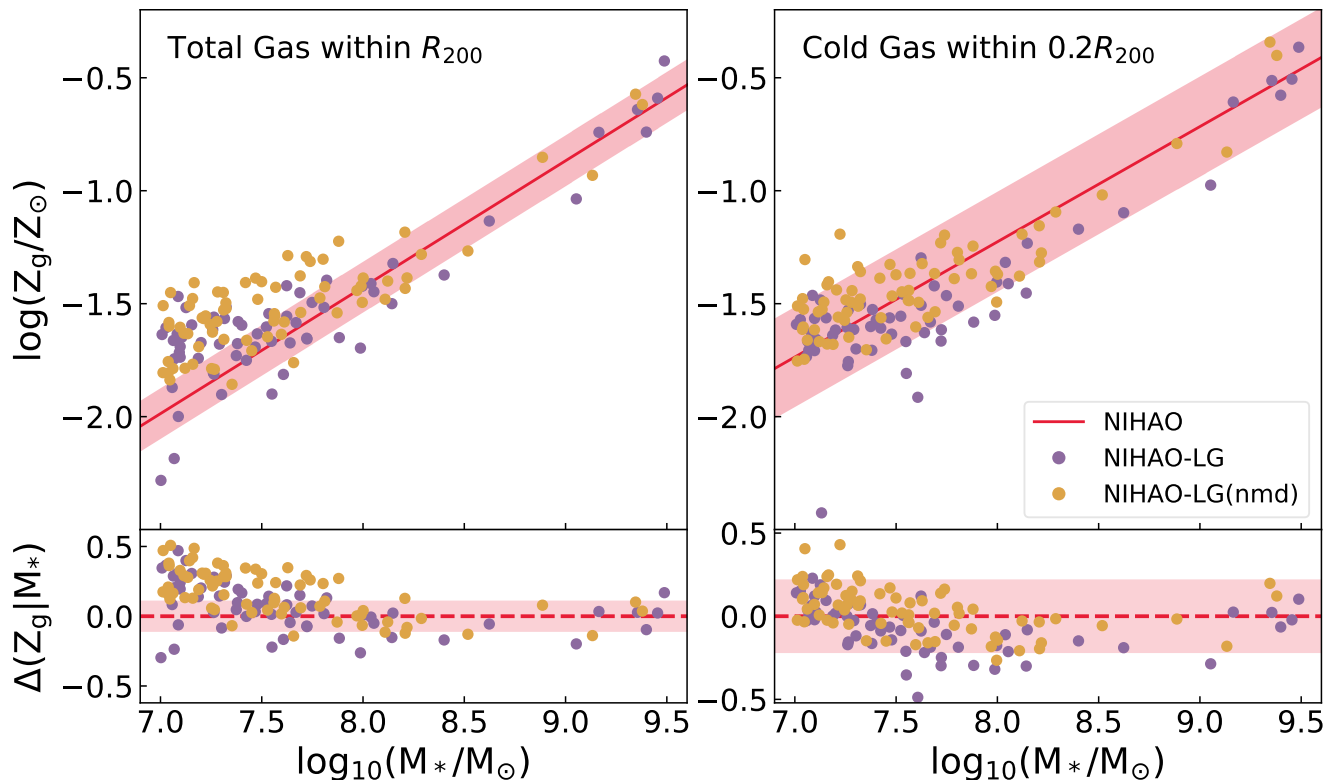


**Figure 4.** Average gas metallicity versus stellar mass for the three simulated dwarf samples. The left-hand panel shows the metallicity for all the gas within  $R_{200}$  and the right-hand panel shows the metallicity for the cold gas within  $0.2R_{200}$ . All other details as in Fig. 3

gas content may not be fully accounted for. A similar difference exists in the comparison of simulated LG dwarfs and the observed data by Peeples et al. (2014). At all stellar masses, LG dwarfs have higher cold gas content than observations. However, given the large error bars at the low mass end for Peeples et al. (2014), a fraction of the simulated LG dwarfs agree with the observations.

In summary, we find that the total gas contents within the field and LG dwarfs show similar distributions. The LG dwarfs, even accompanied by MW/M31, do not gain additional gas that might be generated because of the outflows from the massive halo. However, most gas within the LG dwarfs is found to be cold resulting in a larger cold gas content (especially the low mass dwarfs) compared to field dwarfs. The larger cold gas fraction in LG dwarfs maybe due to the metallicity of the inflowing gas.

Fig. 4 shows a comparison of the gas metallicity between field NIHAO galaxies and the LG dwarf systems. The left-hand and right-hand panels present the average gas metallicity for all the gas within the halo and the average gas metallicity for the cold gas within  $0.2R_{200}$  respectively. The field NIHAO systems have  $Z_g \propto M_*^{0.56 \pm 0.05}$  with a scatter of  $0.12 \pm 0.03$  dex. The LG dwarfs, on the other hand, exhibit a bimodal distribution in the  $Z_g-M_*$ . Low-mass LG dwarfs ( $\log(M_*/M_\odot) \leq 8.0$ ) have a higher, though constant, gas metallicity than field centrals with  $\log(Z_*/Z_\odot) \sim -1.6$ . High-mass LG dwarfs follow the same trend and scatter than field NIHAO galaxies. The higher metallicity in the halo of

low-mass LG dwarfs likely results from the outflows induced in the Local Group by the MW and M31.

The right-hand panel of Fig. 4 shows the cold gas metallicity versus stellar mass for the three simulated dwarf samples. The field sample follows a similar relation to all the gas in the halo, with  $Z_g \propto M_*^{0.50 \pm 0.06}$  but with a larger scatter of  $0.19 \pm 0.04$  dex. The LG dwarf galaxies fall within the field relation, presenting no difference in the central cold gas metallicity as a result of environment. Comparing the left- and right-hand panels of Fig. 4, we conclude that metal rich gas in the LG systems is found at radii greater than  $0.2R_{200}$ . This is indicative of recent inflowing gas for LG dwarf systems which has yet to cool down and be available for star formation. We defer a comparison of field and LG dwarfs in the  $M_g-M_*$  and  $Z_g-M_*$  relations as a function of time to Sec. 4.

### 3.2 Stellar Properties

The mean stellar metallicity versus stellar mass for the three samples of dwarf galaxies at  $z = 0$  can inform us about chemical evolution of the galaxies. Most of the heavy metals were formed within the stars and are distributed into the galaxy via stellar feedback. The left panel of Fig. 5 presents the MZR for all NIHAO and LG simulations and a comparison with the observed relation of Gallazzi et al. (2005). While the observed data are only available for relatively massive systems ( $\log(M_*/M_\odot) \gtrsim 9.0$ ), both NIHAO and LG simulated system match observations well. The MW and M31

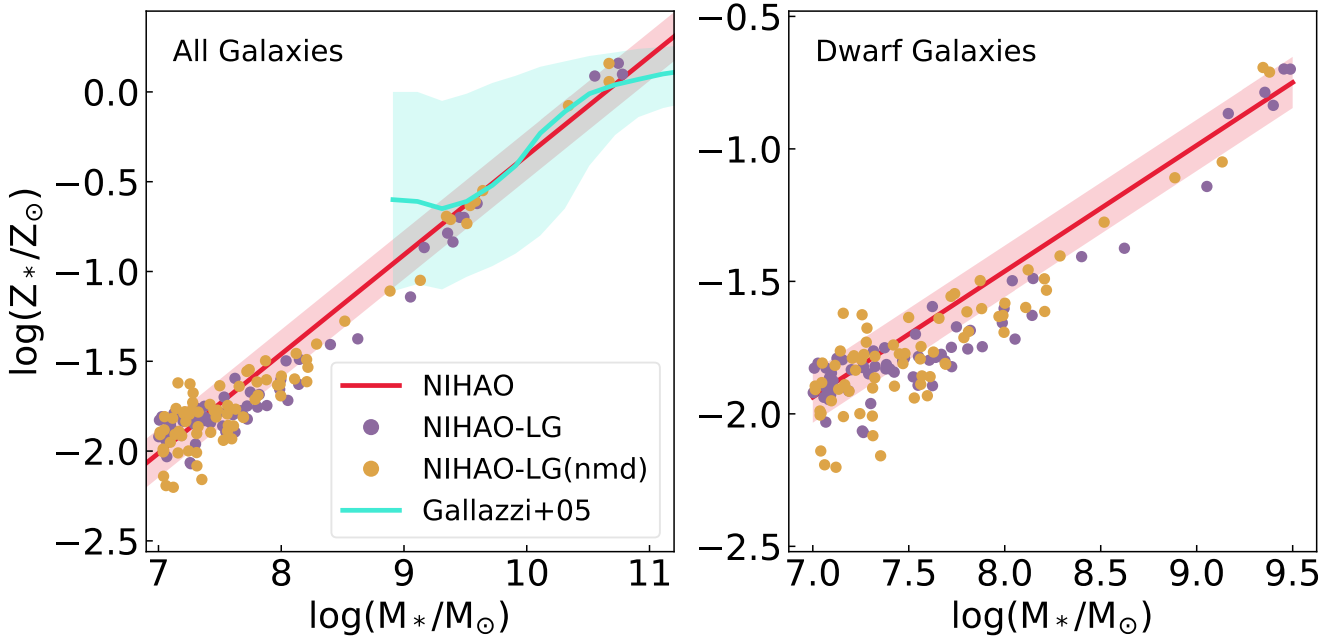


**Figure 5.** Left-hand panel: Stellar metallicity versus stellar mass (MZR) for the complete stellar mass range of NIHAO and LG simulated galaxies at  $z = 0$ . The color scheme is as in Fig. 3. The cyan line and shaded region represent the observed relation from Gallazzi et al. (2005). Right-hand panel: MZR relation zoom-in for the simulated NIHAO and LG dwarf galaxies.

galaxies from both constrained simulations also fall within the observed relation from Gallazzi et al. (2005).

The right panel of Fig. 5 is a zoom-in of the dwarf stellar mass regime. Field dwarfs follow  $Z_* \propto M_*^{0.47 \pm 0.04}$  with a scatter of  $0.09 \pm 0.02$  dex; both LG dwarf simulations have similar median residuals of  $\sim -0.10$  dex. In general, within the broad dispersions of each distribution, the field and LG dwarfs follow two statistically matching distributions. The NIHAO field MZR slope,  $\alpha \simeq 0.47 \pm 0.04$ , the NIHAO-LG(nmd) dwarf relation with a slope of  $\alpha \simeq 0.48 \pm 0.03$ , and the slope for NIHAO-LG,  $\alpha \simeq 0.54 \pm 0.07$ , all fall within statistical errors. The errors calculated for the simulation slopes are standard deviations of 1000 bootstrap runs. Small differences between simulations and observations slope measurements are expected from the sample sizes of our respective studies (Sorice & Guo 2016). While our LG samples contain  $\sim 100$  dwarfs, the observed sample only contains 30 dwarf systems.

Observers typically measure stellar chemical abundance of galaxies using bright metal absorption lines such as those of iron or magnesium. Here we present a comparison of the stellar iron abundances between the three simulated dwarf samples and observations from Kirby et al. (2013). With most of the iron concentrated in the central parts of the galaxies, the average iron abundance weighted by stellar mass encompasses all star particles within the half-light radius. An essential aspect of this chemical comparison is the averaging process for the star particles in the simulation. At first, similar to the observing process, the averaging is carried out with the metallicity in logarithmic

space (Evan Kirby, private communication.). The average iron abundance then becomes,

$$\langle [\text{Fe}/\text{H}] \rangle_{*,\log} = \frac{\sum_i ([\text{Fe}/\text{H}]_{*,i} m_{*,i})}{\sum_i (m_{*,i})}, \quad (1)$$

where  $[\text{Fe}/\text{H}]$  is the iron abundance and  $m_*$  is the stellar mass of the star particle  $i$ . However, the averaging process in logarithmic units is inappropriate. A proper expression for the mean iron abundance is given by

$$\langle [\text{Fe}/\text{H}] \rangle_{*,\text{lin}} = \log \left( \frac{\sum_i (10^{[\text{Fe}/\text{H}]_{*,i}} m_{*,i})}{\sum_i (m_{*,i})} \right). \quad (2)$$

In Eq. (2), the iron abundance per star particle,  $i$ , is calculated in linear space and the logarithm of the complete expression is taken once the average is computed. Our comparison of the simulated dwarf systems uses linear averages (Eq. (2)). For complementarity and comparison with observations, the stellar iron abundances averaged in logarithmic space are also reported.

The left-hand panel of Fig. 6 presents the linearly averaged iron abundance versus stellar mass for the three simulated dwarfs samples. Field dwarf galaxies from NIHAO follow  $\langle [\text{Fe}/\text{H}] \rangle \propto M_*^{0.36 \pm 0.04}$  with a scatter of  $0.09 \pm 0.02$  dex. The NIHAO-LG(nmd) dwarfs and field galaxies have an identical distribution, and NIHAO-LG low mass dwarfs are somewhat poorer in metals than the field. A linear average for the stellar iron abundance is preferentially biased



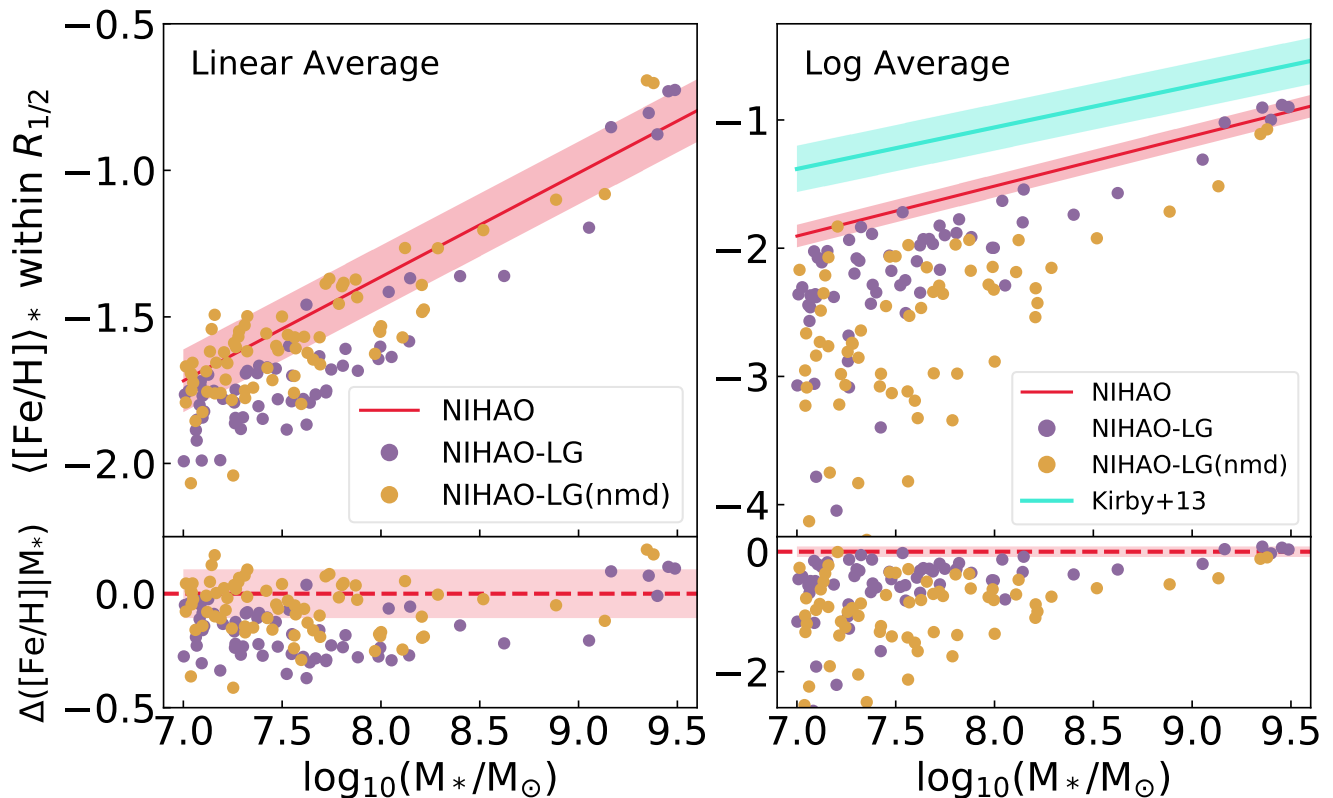


**Figure 6.** Iron abundance,  $\langle [\text{Fe}/\text{H}] \rangle_{*}$ , versus stellar mass for the three samples of simulated dwarf galaxies. The color scheme is as in Fig. 3.  $\langle [\text{Fe}/\text{H}] \rangle_{*}$  was averaged over all stellar particles within  $R_{1/2}$ . The left-hand panel shows the mass-weighted averages carried out in linear space (see Eq. (2) for definition) while the right-hand panel shows mass-weighted averages calculated in log space (see Eq. (1) for definition). In cyan, the right-hand panel shows the observed relation for Local Group dwarf galaxies from Kirby et al. (2013).

towards metal rich stars. With the “no metal diffusion” feature removed from NIHAO-LG(nmd), metal-rich stars form more easily resulting in higher stellar iron abundances than NIHAO-LG.

The presence of massive spirals like the MW and M31 around these dwarfs can lead to strong outflows, likely leading to metal-enriched stellar populations in LG dwarfs. However, contrary to this expectation, NIHAO-LG shows metal-poor stellar populations relative to field systems. Given the deep potential of the MW and M31, a significant fraction of the outflowing gas and metals may turn up with a galactic fountain and be retained by the massive halo. Such an effect can yield a metal-poor stellar population for the LG dwarfs relative to field centrals. The impact of pre-enrichment due to MW/M31 may erode leading to similar stellar populations within the field and LG. Our result in the left-hand panel of Fig. 6 is quantitatively similar to that of FIRE (Escala et al. 2018) or the high-resolution NIHAO simulations (Buck et al. 2019).

The right-hand panel of Fig. 6 shows the logarithmic averaged stellar iron abundance for the three simulated dwarf samples and observed relation from Kirby et al. (2013). With a different averaging technique comes a revised relation; the field galaxies relation,  $\langle [\text{Fe}/\text{H}] \rangle_{*}-M_{*}$ , is now slightly steeper and tighter with a slope of  $0.39 \pm 0.04$  and scatter  $0.09 \pm 0.02$ . The differences between linear and logarithmic averaging of

the  $\langle [\text{Fe}/\text{H}] \rangle_{*}-M_{*}$  relations are still well within the errors. The observed relation shows similar linear slope ( $0.30 \pm 0.02$ ) but with a larger scatter ( $0.17$  dex) and lower zero-point. The simulated field galaxies from NIHAO are more iron-poor, as is expected for these low mass galaxies who cannot retain metal-rich gas due to stellar feedback and winds. The simulated LG dwarfs show an even poorer metal content in stars, with their  $[\text{Fe}/\text{H}]$  distribution lower than observations by a factor 15. The three simulations and observations differ only in their zero-point offset (the trends have the same slope) which is directly linked to the implementation of supernovae feedback in the simulations (Escala et al. 2018). The study of Buck et al. (2021) provides an improved chemical enrichment scheme for NIHAO simulations that should yield a better match with observations. We shall return to such data-model comparison in a future study. Fig. 3 shows the excess cold gas mass in LG dwarfs compared to field dwarfs. That excess gas dilutes metal production through stellar evolution and yields a metal-poorer stellar populations in LG dwarfs. Figs. 5 and the left-hand panel of Fig. 6 tell a similar story.

Finally, Tab. 2 presents a quantitative summary of our comparisons of field and LG dwarf populations. For the scaling relations used here, the slope, zero-point, and scatter for the field NIHAO populations are shown. The average difference between the LG and field dwarf populations is also

Scaling Relation (1)	NIHAO			NIHAO-LG	NIHAO-LG(nmd)
	Slope (2)	Zero-point (3)	Scatter (4)	Average Difference [dex] (5)	Average Difference [dex] (6)
$M_{\text{gas}} - M_*$	$0.73 \pm 0.09$	$3.47 \pm 0.73$	$0.30 \pm 0.06$	$0.00 \pm 0.05$	$0.03 \pm 0.06$
$M_{\text{coldgas}} - M_*$	$1.09 \pm 0.15$	$0.12 \pm 1.27$	$0.46 \pm 0.10$	$0.41 \pm 0.11$	$0.49 \pm 0.09$
$Z_{\text{gas}} - M_*$	$0.56 \pm 0.05$	$-5.92 \pm 0.37$	$0.12 \pm 0.03$	$0.18 \pm 0.06$	$0.26 \pm 0.06$
$Z_{\text{coldgas}} - M_*$	$0.50 \pm 0.06$	$-5.24 \pm 0.49$	$0.19 \pm 0.04$	$0.00 \pm 0.04$	$0.08 \pm 0.03$
$Z_* - M_*$	$0.47 \pm 0.04$	$-5.25 \pm 0.31$	$0.09 \pm 0.02$	$0.02 \pm 0.03$	$0.07 \pm 0.02$
$\langle [\text{Fe}/\text{H}] \rangle_* - M_*$	$0.36 \pm 0.04$	$-4.29 \pm 0.31$	$0.09 \pm 0.02$	$0.09 \pm 0.03$	$0.03 \pm 0.03$

**Table 2.** Summary of the scaling relations used for comparison of the three different simulated dwarf populations. Column (1) lists the scaling relation; columns (2-4) present the slope, zero-point and scatter, respectively for the NIHAO dwarfs (acting as the field population); and columns (5-6) show the average difference between the NIHAO field and LG dwarf populations from the constrained simulations. If the values in columns 5 and/or 6 are greater than the scatter of the NIHAO field scaling relations (column 4), the LG dwarf population is considered statistically different. The errors are bootstrapped over 2000 runs.

presented in Tab. 2. That difference is calculated by randomly sampling the same number of LG dwarfs as the field dwarfs (see Tab. 1) and calculating the median residual with respect to the field galaxy scaling relation. This process is bootstrapped 2000 times to estimate the error of the average difference. Tab. 2 reiterates the larger differences in the gas properties of the LG dwarfs relative to field systems. The stellar properties of the LG dwarfs show little to no difference with field galaxies.

### 3.3 Star Formation Rates

Fig. 7 shows the present-day Star Formation Main Sequence (SFMS) for the three samples of simulated galaxies in this study. Our robust measurements of star formation rates (SFR) used the average SFR over the last 100 Myr. The central field galaxies from the NIHAO sample are shown as a best-fit line and shaded region representing the  $1 - \sigma$  region; the constrained LG simulations are shown as colored circles; SFR- $M_*$  measurements for the MW and M31 from Yin et al. (2009) and Bland-Hawthorn & Gerhard (2016), as well as observed SFMS studies from Calzetti et al. (2007), Davies et al. (2016) and Cluver et al. (2017) are also shown as coloured lines for comparison.

The  $1 - \sigma$  scatter for these observed relations are in the lower right corner of the plot as point with error bars. For this discussion of the SFMS, the full stellar mass range is used for the simulated sample. The simulated NIHAO sample follows  $\text{SFR} \propto M_*^{0.76 \pm 0.08}$  with a scatter of 0.50 dex. This agrees well with the observed relations along with their scatter; however, the scatter of the simulated relation exceeds the observed scatter by 0.2 dex.

The massive galaxies ( $\log(M_*/M_\odot) > 9.5$ ) for both constrained LG samples fall within the  $1 - \sigma$  region of the NIHAO field galaxies relation. The dwarf galaxies ( $\log(M_*/M_\odot) < 9.5$ ) in the constrained LG simulations show slightly lower SFRs compared to their field dwarf companions. Most LG dwarfs, from both simulations, are not star-forming galaxies at present day. Most of the LG dwarfs contain mainly older stellar populations; nearly 50 per cent of the LG dwarfs (in NIHAO-LG and NIHAO-LG(nmd)) have formed half of their present stellar mass in the first  $\sim 5$  Gyr. In general, LG and field NIHAO galax-

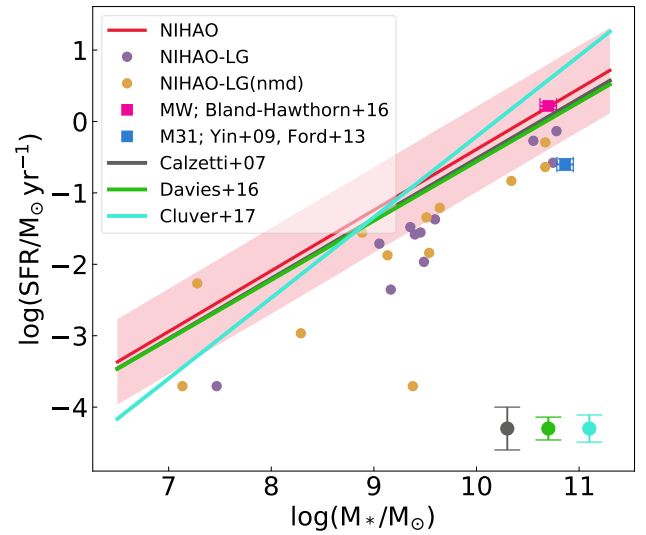


**Figure 7.** The SFMS at redshift  $z = 0$  for the three samples of simulated galaxies. The color scheme follows Fig. 3. The NIHAO central galaxies are presented as the best-fit with the shaded region representing  $1\sigma$  scatter in the relation. The gray, green and cyan lines show mid-infrared SFMS inferred by Hall et al. (2018) for Calzetti et al. (2007), Davies et al. (2016), and Cluver et al. (2017). The points with error bars in the lower right corner represent the scatter of these observed relations. Also shown are the recent SFRs and stellar masses for the MW (Bland-Hawthorn & Gerhard 2016) and M31 (Yin et al. 2009; Ford et al. 2013) as pink and blue squares, respectively.

ies follow the same distribution, in agreement with recent empirical renditions of the SFMS. We also note the large differences between observed relations presented in Davies et al. (2016) and Cluver et al. (2017). Those are mainly due to the variations in sample sizes; Davies et al. (2016) used 3749 galaxies from the GAMA sample (Driver et al. 2016) while Cluver et al. (2017) used only 79 galaxies from the SINGS/KINGFISH survey (Kennicutt et al. 2003, 2011).

Fig. 7 includes observed measurements of SFR and  $M_*$  for the MW (Bland-Hawthorn & Gerhard 2016) and M31 (Yin et al. 2009; Ford et al. 2013). These, along with the sim-

Halo/Simulation (1)	SFR [ $M_{\odot} \text{ yr}^{-1}$ ] (2)	$M_{*}$ [ $10^{10} M_{\odot}$ ] (3)
M31 (NIHAO-LG)	0.27	5.57
M31 (NIHAO-LG(nmd))	0.23	4.66
M31 (Observed)	$0.25_{0.04}^{0.06}$	5.9 – 8.7
MW (NIHAO-LG)	0.73	6.02
MW (NIHAO-LG(nmd))	0.51	4.69
MW (NIHAO; <b>g8.26e11</b> )	2.05	4.68
MW (Observed)	$1.65 \pm 0.19$	$5.0 \pm 1.0$

**Table 3.** Present SFR and  $M_{*}$  measurements for the MW and M31 from our constrained LG simulations and observation. Column (1) gives the halo and simulations, while columns (2) and (3) give the SFR and  $M_{*}$  in units of  $M_{\odot} \text{ yr}^{-1}$  and  $10^{10} M_{\odot}$ , respectively. Observed measurements for MW (Bland-Hawthorn & Gerhard 2016) and M31 (Yin et al. 2009; Ford et al. 2013) are also presented.

ulated properties, are also presented in Tab. 3. Once again, the stellar masses for the MW and M31 from the LG simulations are in broad agreement with the observed estimates and **g8.26e11** (a Milky-Way analog from the NIHAO simulations).

The SFR, on the other hand, shows more variability. The simulated LG M31 halos agree with observed SFR from Ford et al. (2013) who used far ultraviolet and  $24\mu\text{m}$  emission measurements for their estimates of the global SFR =  $0.25_{0.04}^{0.06} M_{\odot} \text{ yr}^{-1}$  for M31. However, the LG MW halos under-predict the SFRs relative to observed measurements. For instance, Bland-Hawthorn & Gerhard (2016) reported SFR =  $1.65 \pm 0.19 M_{\odot} \text{ yr}^{-1}$  from calculations by Licquia & Newman (2015) and assuming a Kroupa Initial Mass Function (IMF). The assumption of the underlying IMF is always a significant source of error in the calculation of SFR (Hennebelle & Chabrier 2013).

NIHAO halo **g8.26e11** (presented in Tab. 3) over-predict the SFR relative to the observed MW SFR, whereas the observed and simulated values agree within  $2\sigma$ . However, while the high SFR value for **g8.26e11** disagree with the constrained LG simulations and observations, they still fall within the  $1 - \sigma$  scatter of the field SFMS. The field relation, and therefore **g8.26e11**, also agrees with the observed SFMS relations of Calzetti et al. (2007), Davies et al. (2016) and Cluver et al. (2017).

#### 4 EVOLUTION OF THE LOCAL GROUP

We have found so far that the properties of simulated field and LG dwarf galaxies at low redshift ( $z = 0$ ) showed small, though non-negligible, differences at low redshift. LG dwarfs have larger (0.2 dex) stellar masses and a larger (0.35 dex) cold gas content within  $0.2R_{200}$  than field dwarfs at  $z = 0$ . The hot gas content for LG dwarfs is also more metal rich than field systems. In this section, we study the evolution of various galaxy properties in an attempt to isolate, if present, evolutionary differences between LG and field dwarf systems.

Motivated by our objective to study pre-enrichment in LG dwarfs due to co-evolution with MW and M31, we shall first examine the outflowing gas properties from the most massive halos in the two constrained LG simulations and

NIHAO. We will then trace the evolution of some key dwarf galaxy scaling relations with time. In doing so, we wish to isolate specific times in the evolutionary history of LG and correlated with the evolution of the MW and M31. Ultimately, we wish to constrain the influence of massive galaxies on the evolution of LG dwarfs. Given our two constrained LG simulations, we can also address the influence of metal diffusion in simulations.

##### 4.1 MW/M31

The mass of outflowing gas in the two constrained LG simulations and as a function of time or redshift can inform us about star formation driven outflows which can be correlated with inflows in LG dwarfs. This is shown in the left-hand panel in Fig. 8. The gas mass is calculated within a spherical shell between  $1.5R_{\text{vir}} \leq r \leq 2R_{\text{vir}}$  and with radial velocity  $v_r > 0 \text{ km s}^{-1}$ . The evolution of both constrained LG simulations with time is nearly identical until  $\sim 5 \text{ Gyr}$ , with a gentle decrease in outflowing gas mass by  $\sim 0.2 \text{ dex}$ . Differences become noticeable after  $\sim 5 \text{ Gyr}$  where the trends diverge; outflowing gas decreases by 0.2 dex for NIHAO-LG(nmd) but increases by 0.1 dex for NIHAO-LG. These different trends between NIHAO-LG and NIHAO-LG(nmd) stem from slightly different SFH between the halos from the LG constrained simulations. At  $z \leq 1$ , the most massive halo in NIHAO-LG(nmd) shows a  $\sim 0.1 \text{ dex}$  lower SFR compared to NIHAO-LG (see right-hand panel for Fig. 8). The outflowing gas content for the two halos in Fig. 8 agree from  $z \sim 0.1$  to the present time.

Similar conclusions are drawn from the center panel of Fig. 8 which shows the outflowing gas metals from the most massive halo in the constrained LG simulations. Both constrained LG halos expel a similar metal content in their outflowing gas. The differences in outflowing metals is directly correlated to the higher SFR for the LG halos presented in the right-hand panel for Fig. 8. The higher SFR leads to enhanced feedback and enriched outflows. Between  $z \sim 2 - 0.5$ , as a result of metal diffusion, the most massive halo from NIHAO-LG expels relatively metal-poor gas. The metallicity of gas particles in NIHAO-LG simulation will decrease as it interacts with the environment due to the inclusion of metal diffusion, resulting in lower overall metallicity.

In all three panels of Fig. 8, the massive halos from both constrained LG simulations depict very similar evolution history. Varying subgrid physics implementations, including/excluding metal diffusion in our cases, does not lead to significant changes to the MW/M31 galaxy properties and therefore surrounding dwarfs. In general, the most massive halos from both constrained LG simulations present very similar outflowing gas properties. For massive halos, the presence or absence of metal diffusion does not affect the galaxy population properties.

##### 4.2 Dwarf Galaxies

We turn our attention to the time evolution of the LG and field dwarf systems using galaxy scaling relations presented in Sec. 3. The co-evolution of LG dwarfs with the MW/M31 should be apparent in the gas properties of the LG dwarfs relative to the field systems. The full set of LG and field

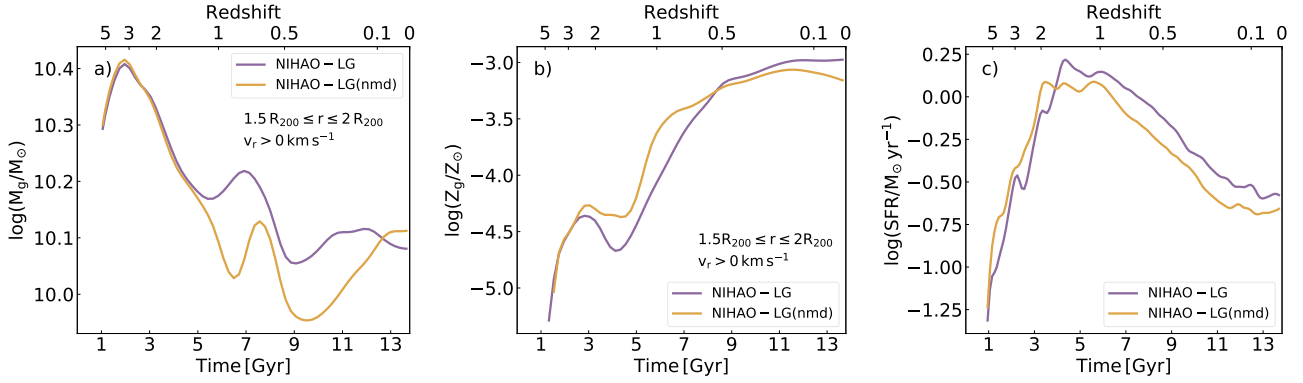


**Figure 8.** Total outflowing gas mass (left-hand panel) and gas metals (center panel) within a spherical shell of  $1.5R_{\text{vir}} \leq r \leq 2R_{\text{vir}}$  as function of time for the most massive halo in the two constrained LG simulations (purple and gold lines). The right-hand panel shows the SFH of the two LG halos. Redshifts are shown on the top x-axis.

dwarfs at all redshifts are compared using the average residual from the field galaxy scaling relations. The average residual for the constrained LG simulations is:

$$\langle \Delta(y_{\text{LG}}|M_*) \rangle_{\text{LG}}(t) = \langle y_{\text{LG}}(t) - (\alpha_{\text{N}}(t)M_{*,\text{LG}}(t) + c_{\text{N}}(t)) \rangle, \quad (3)$$

where  $y_{\text{LG}}$  is a galaxy property presented in Sec. 3,  $\alpha_{\text{N}}(t)$  and  $c_{\text{N}}(t)$  are the slope and intercept of the fitted scaling relation from the field NIHAO sample,  $M_{*,\text{LG}}(t)$  is the stellar mass of the LG system, and all properties are calculated at time  $t$ . The variables on the right-hand side of Eq. (3) all yield the average residual at time  $t$ ,  $\langle \Delta(y_{\text{LG}}|M_*) \rangle_{\text{LG}}(t)$ . The error on the average residuals are calculated as  $\epsilon_{\text{LG}} = \sigma(y_{\text{LG}}|M_*)/\sqrt{N}$ ; where  $\sigma(y_{\text{LG}}|M_*)$  is the standard deviation of the residual from the field scaling relation and  $N$  is the number of data points. In this formalism, we define the LG and field dwarfs as different galaxy populations when  $\epsilon_{\text{N}} < \langle \Delta(y_{\text{LG}}|M_*) \rangle_{\text{LG}}(t)$  where  $\epsilon_{\text{N}}$  is the error of the linear fit to the NIHAO galaxies. In this comparison of the LG and field dwarfs, the scatter of the field galaxy scaling relations is also presented. Due to evolution in time, the slopes of nearly all scaling relations vary; therefore, the forward scatter ( $\sigma_{\text{N},f}$ ) alone is not a robust comparison metric. Instead, we use the orthogonal scatter, defined as  $\sigma_{\text{N}} = \sigma_{\text{N},f}/\sqrt{1 + \alpha_{\text{N}}^2}$ , for our comparisons.

#### 4.2.1 Gas Content

We study the evolution of gas properties, in particular mass and metallicity, for both field and LG dwarfs. A comparison of the mass and/or metallicity of the total and/or gas in the LG halos with the field systems, can provide evidence of the pre-enrichment of LG dwarfs from the more massive halos in the constrained LG simulations. Fig. 9 shows the comparison of the field and LG systems as a function of time for the  $M_g - M_*$  relation. The top and bottom panels show all total gas content within  $R_{200}$  and the cold gas content within  $0.2R_{200}$ , respectively. The orthogonal scatter in the total  $M_g - M_*$  relation increases from  $\sim 0.11$  dex, at  $z \sim 3.2$ , to 0.26 dex, at present day. The slope of the relation, however, shows little change over time.

Both LG and field dwarfs have the same distribution for the total gas content for the complete evolutionary history as the purple and gold error band follow the dark red

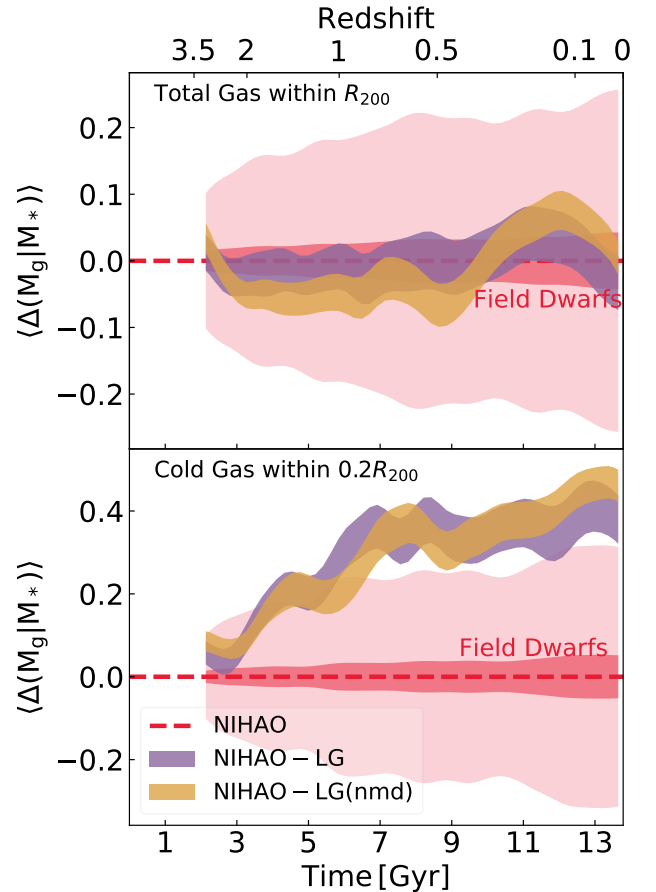


**Figure 9.** Evolution in the residual for the gas mass - stellar mass relation as a function of redshift for dwarf galaxies with  $(7.0 \leq \log(M_*/M_\odot) \leq 9.5)$  for the two constrained LG simulations shown as coloured bands (purple and gold). The gas mass - stellar mass relation of NIHAO central dwarfs is the horizontal line at  $\langle \Delta(M_{\text{Gas}}|M_*) \rangle = 0.0$ , the dark red region present the error on the average relation, and the lighter shaded region showing the  $1 - \sigma$  scatter of the scaling relation at each redshift. The top and bottom panels show the total and cold gas mass, respectively. The redshift is represented on the top x-axis.

shaded region (see Fig. 9). The field systems occupy the central regions of their respective dark matter halo and are fed gaseous material from the cosmic filaments, major/minor gas rich mergers. The LG dwarfs accumulate their gas content predominantly by the outflows from the larger halos (MW/M31). The outflows from the larger halos, in the constrained simulations, are substantial enough to build up the gas content similar to the central field dwarfs.

While the evolution of the total gas content of the LG and field systems is very similar, the slope and the scatter of the cold  $M_g-M_*$  relation in the field evolve significantly as a function of time (bottom panel of Fig. 9). The slope changes range from 0.80 at  $z \sim 3.2$  to 1.10 at present day, while the scatter grows from 0.09 dex at  $z \sim 3.2$  to 0.31 dex at  $z = 0$ . Furthermore, most of the gas within the LG dwarf is cold gas within  $0.2R_{200}$ . The difference in the cold gas mass between field and LG dwarfs continues to increase from  $z \lesssim 2$  to present day. At  $z = 0$ , the LG dwarfs contain 0.4 dex more cold gas within  $0.2R_{200}$  than the field systems. The increasing cold gas mass in the LG dwarfs, compared to the field, is evidence of the co-evolution with MW/M31. The star formation episodes and interactions with MW/M31 allow for the build-up of cold gas content, and therefore provide excess fuel for star formation, in the LG dwarfs populations.

#### 4.2.2 Chemical Content

The chemical content of gas in LG dwarf halos can inform us about the origin of the gas content. A similar chemical content as the field dwarfs for the LG system could indicate that the evolution history of dwarfs is independent of the environment. Fig. 10 shows the metallicity of the gas content in the field and LG samples. The format of Fig. 10 is the same as Fig. 9. In the top panel, where gas metallicity of total gas content is computed within  $R_{200}$ , field dwarfs display little variation in the scatter of the  $Z_g-M_*$  relation. The two constrained LG simulations behave slightly differently with time, though both simulations show more metal rich gas than the field systems.

From  $z \sim 1$  to present day, the NIHAO-LG dwarfs possess a higher metal rich gas content (by 0.15 dex; which is  $3 - \sigma$  different from the field). While the total gas mass of the field and LG dwarfs evolve in similar ways (see top panel of Fig. 9), the gas content of the LG dwarfs is significantly more enriched. The metal enriched gas in these LG dwarfs is a direct consequence of outflows generated by the MW/M31 halo. The metal build-up in NIHAO-LG dwarfs is related to the peak of metal rich gas outflowing from the most massive halo (see left-hand and center panels of Fig. 8). The metal rich content of the inflowing gas from MW/M31 allows for it to cool down on shorter timescales (than fresh, metal poor gas in field dwarfs) and be available for further star formations events. Such star formation events would allow for the LG dwarfs to build up their stellar mass. Field dwarf systems, on the other hand, have access to metal enriched gas mostly through the mergers.

The excess metal rich gas is more pronounced in NIHAO-LG(nmd) compared to NIHAO-LG and field NIHAO systems. The gas content in LG dwarfs from NIHAO-LG(nmd) are nearly 0.3 dex (or  $5 - \sigma$  different) more enriched than field systems. The absence of metal diffusion in NIHAO-LG(nmd) leads to gas particles building up their

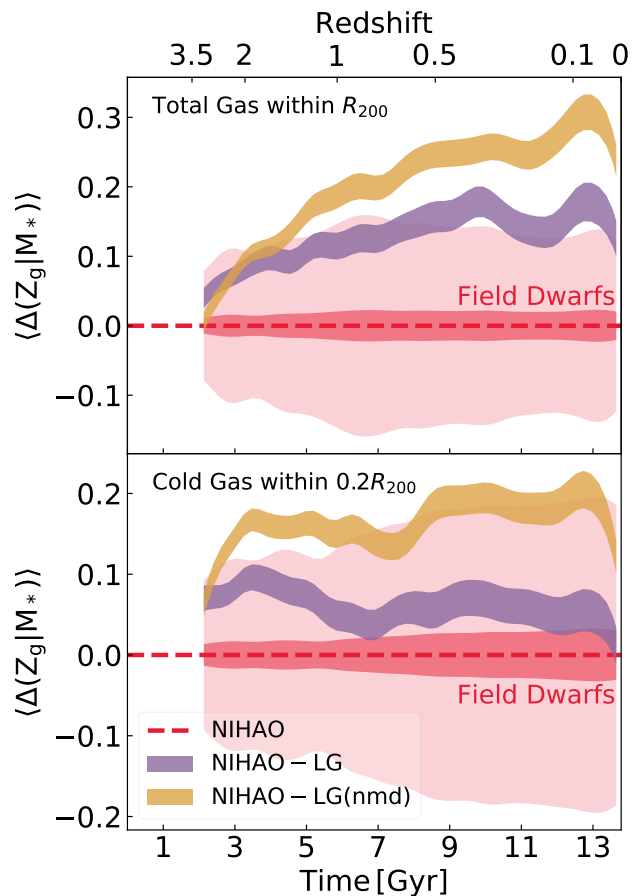


Figure 10. Same as Fig. 9 but for gas metallicity.

metal content and thus yields systematically higher metallicities. Similar signatures are seen at  $z = 0$  in Fig. 4 with more metal rich gas in NIHAO-LG compared to NIHAO-LG(nmd).

The bottom panel in Fig. 10 depicts the cold gas metals within the three sample of dwarfs. Unlike the  $Z_g-M_*$  relation for total gas, the cold gas  $Z_g-M_*$  relation for the field shows increasing scatter as a function of time. Once again, the two constrained LG simulations behave differently; NIHAO-LG(nmd) dwarfs at all times have the same distribution as the field systems, whereas NIHAO-LG dwarfs for their complete history lie  $1 - \sigma$  scatter above from the field systems. The excess metal in the gas within the halo translates into metal-rich cold gas within  $0.2R_{200}$ . The metal rich hot gas flowing in from MW/M31 due to intense periods of star formation quickly contributes to building up the cold gas content in the LG dwarfs. However, both NIHAO-LG and NIHAO-LG(nmd) show marginal evolutionary differences from the field dwarfs. The lack of evolution of the cold gas metallicity could be linked to the lack of star formation in LG dwarfs. Nearly 70 percent of the LG dwarfs (both NIHAO-LG and NIHAO-LG(nmd)) are quenched by the first 4.5 Gyr of their formation. A quenched star formation hinders the recycling of metals in gas and yields a static metal content in the LG cold gas.

## 5 SUMMARY AND CONCLUSIONS

The Local Group offers us with a superb laboratory for the study of the formation and evolution of the dwarf galaxies; the most abundant cosmological structures in the Universe. The main question that we have addressed here is to what extent this laboratory can be used to teach us about galaxy formation at large and its cosmological implications. In this comparative study, we have highlighted the similarities and differences between simulated LG and field dwarf galaxies as a function of time/redshift and a comparison with observations. This comparison relied on dwarf halos from the NIHAO high resolution zoom-in simulations as our field control sample. For the LG dwarfs, we present and analysed the constrained LG simulations run with NIHAO hydrodynamics. To further analyse the role of chemical evolution in LG dwarfs, two different LG constrained simulations were used; with and without metal diffusion.

Present-day field and LG dwarfs were found to have similar stellar populations but significantly different gas contents. While the total gas content of dwarfs is not influenced by environment (Sawala et al. 2012), a larger fraction of the gas within LG dwarfs is cold and resides within  $0.2R_{200}$ . The latter is correlated to the higher metal content (than field dwarfs) of the gas in the halo. The higher gas metal content of the LG dwarfs is accumulated via interactions with the host halos (MW/M31) which allows the LG dwarfs to collect the heavy metal generated during peak star formation episodes of the host halos. High metallicity allows for shorter cooling times and is available for star formation episodes and further metal processing in the LG dwarfs. However, such episodes in LG dwarfs lead to strong feedback events and force metals out of the galaxy (where stars reside) while still being locked in the halo. The time evolution of the cold gas mass within LG dwarfs shows departures from the field sample around  $z \sim 1 - 2$ . This also coincides with the peak in the SFH of the most massive host halos in our constrained LG simulations. Close passage of the LG dwarfs around the host halos would allow for the accumulation of the higher metal-rich gas content (eg. Di Cintio et al. 2021).

However, relative to field systems, LG dwarfs show little evolution in cold gas metallicity with time. While the higher metallicity in the halo should allow for gas to cool down efficiently and lead to SF events, stellar feedback and outflows in the dwarfs will suppress any episodes and further stellar evolution leading to a quenched system. Therefore, the stellar and cold gas evolution of LG dwarfs is strongly dictated by in-situ processes such as stellar feedback, winds and photoevaporation due to re-ionization, more so than environmental processes (Sawala et al. 2012). A significant fraction of the dwarfs in our constrained LG simulations build up their stellar content early in their evolution history and remain quenched thereafter (eg. Sand et al. 2010; Simon et al. 2021). The LG and field have, therefore, similar galaxy populations; esp. in stellar properties.

We also found that changing the metal diffusion sub-grid prescription does not affect the gas mass within the LG dwarfs through their complete evolution histories. However, the LG simulation with metal diffusion results in a metal poor gas content, by  $\sim 0.1$  dex relative to no metal diffusion simulation. This is expected as metal diffusion drives the metallicity of gas particles closer to the average metallicity.

The average metallicity of stellar particles at  $z = 0$  does not change after including metal diffusion. Both constrained LG simulations produce stellar metallicities in agreement with simulated field dwarfs and observations. The average iron abundance in LG simulations show only marginal differences due to metal diffusion, albeit less pronounced. At  $z = 0$ , the stellar iron abundances in the two constrained LG simulations differ by  $\sim 0.05$  dex (left-hand panel of Fig. 6). However, the difference is only found in the offsets while the slope of the stellar mass – iron abundance relations are similar for field and LG dwarfs. The simulated stellar mass – iron abundance relation also showed no dependence with environment and appears to be regulated by in-situ processes such as feedback and photoevaporation (Skillman et al. 1989; Escala et al. 2018). The different normalizations are likely related to the manner by which supernovae feedback are modelled in the simulations.

Finally, we also compared the SHMR between field and LG dwarfs (see Fig. 1). We found that, for the same halo mass, both constrained LG simulations have larger stellar contents than field systems. The larger stellar content relative to the total mass is likely due to enrichment from larger halos allowing for gas to cool down efficiently. and interactions with the host halos inducing star burst events (Munshi et al. 2017; Buck et al. 2020).

Local Group dwarf galaxies possess very similar stellar properties to those found in the field. Field and LG dwarfs had early bursts of star formation but remain quenched for the rest of their history. The evolution of their stellar properties is strongly dictated by in-situ processes and less so by environmental processes. On the other hand, the gas properties of LG dwarfs show signs of pre-enrichment from the host halos, with the larger cold gas mass and metal content being directly associated with the outflows generated by the MW and/or M31. Given the similar stellar properties of simulated dwarfs, high-resolution dwarf simulations such as NIHAO (Wang et al. 2015) and FIRE (Garrison-Kimmel et al. 2019) may then be used to analyse the general dwarf population. Our results have demonstrated the value of LG observations, specifically their stellar properties, to be used as constraints for the overall dwarf populations in our Universe. The Local Group provides us with a powerful and most valuable laboratory for understanding galaxy formation and evolution processes nearby. The unique aspects seen in the gas properties of the LG can be examined using high-resolution constrained LG simulations (Gottloeber et al. 2010; Sorce et al. 2016; Carlesi et al. 2016; Libeskind et al. 2020). Furthermore, with the advent of next generation telescopes such as JWST, Euclid, Rubin/LSST, and SKA, observational signatures of pre-enrichment can ultimately be teased out of high redshift LG analogs and their accompanying dwarfs.

## DATA AVAILABILITY

The data underlying this article will be shared upon request to the corresponding author(s).

## ACKNOWLEDGEMENTS

NA and SC are grateful to the Natural Sciences and Engineering Research Council of Canada and Queen's University for generous support through various scholarships and grants. TB also acknowledges support from the European Research Council under ERC-CoG grant CRAGSMAN-646955. NIL acknowledges financial support from the Project IDEXLYON at the University of Lyon under the Investments for the Future Program (ANR-16-IDEX-0005) GY thanks the Spanish Ministry of Science, Innovation and Universities (MICIU/FEDER) for financial support under research grant PGC2018-094975-C2. YH has been partially supported by the Israel Science Foundation grant ISF 1358/18. Barbara Catinella, Luca Cortese and Ananthan Karunakaran provided valuable references for our observational comparisons to simulated data. Aaron Dutton is also thanked for earlier contributions and comments relevant to this work. The research was performed using the PYNBODY package (Pontzen et al. 2013), SCIPY (Virtanen et al. 2020), NUMPY (Harris et al. 2020) and used MATPLOTLIB (Hunter 2007) for all graphical representation. The authors gratefully acknowledge the Gauss Centre for Supercomputing e.V. (www.gauss-centre.eu) for funding this project by providing computing time on the GCS Supercomputer SuperMUC at Leibniz Supercomputing Centre (www.lrz.de). This research was carried out on the High Performance Computing resources at New York University Abu Dhabi. We greatly appreciate the contributions of all these computing allocations.

## REFERENCES

- Aihara H., et al., 2011, *ApJS*, **193**, 29
- Behroozi P. S., Wechsler R. H., Conroy C., 2013, *ApJ*, **770**, 57
- Benítez-Llambay A., Navarro J. F., Abadi M. G., Gottlöber S., Yepes G., Hoffman Y., Steinmetz M., 2015, *MNRAS*, **450**, 4207
- Benítez-Llambay A., Navarro J. F., Abadi M. G., Gottlöber S., Yepes G., Hoffman Y., Steinmetz M., 2016, *MNRAS*, **456**, 1185
- Bland-Hawthorn J., Gerhard O., 2016, *ARA&A*, **54**, 529
- Blank M., Meier L. E., Macciò A. V., Dutton A. A., Dixon K. L., Soliman N. H., Kang X., 2021, *MNRAS*, **500**, 1414
- Blanton M. R., Moustakas J., 2009, *ARA&A*, **47**, 159
- Bradford J. D., Geha M. C., Blanton M. R., 2015, *ApJ*, **809**, 146
- Brinchmann J., Charlot S., White S. D. M., Tremonti C., Kauffmann G., Heckman T., Brinkmann J., 2004, *MNRAS*, **351**, 1151
- Brown T. M., et al., 2012, *ApJ*, **753**, L21
- Buck T., 2020, *MNRAS*, **491**, 5435
- Buck T., Macciò A. V., Obreja A., Dutton A. A., Domínguez-Tenreiro R., Granato G. L., 2017, *MNRAS*, **468**, 3628
- Buck T., Macciò A. V., Dutton A. A., Obreja A., Frings J., 2019, *MNRAS*, **483**, 1314
- Buck T., Obreja A., Macciò A. V., Minchev I., Dutton A. A., Ostriker J. P., 2020, *MNRAS*, **491**, 3461
- Buck T., Rybizki J., Buder S., Obreja A., Macciò A. V., Pfrommer C., Steinmetz M., Ness M., 2021, arXiv e-prints, p. arXiv:2103.03884
- Calzetti D., et al., 2007, *ApJ*, **666**, 870
- Carlesi E., et al., 2016, *MNRAS*, **458**, 900
- Chabrier G., 2003, *PASP*, **115**, 763
- Clemens M. S., Bressan A., Nikolic B., Alexander P., Annibali F., Rampazzo R., 2006, *MNRAS*, **370**, 702
- Cluver M. E., Jarrett T. H., Dale D. A., Smith J. D. T., August T., Brown M. J. I., 2017, *ApJ*, **850**, 68
- Cluver M. E., et al., 2020, *ApJ*, **898**, 20
- Danieli S., van Dokkum P., Conroy C., 2018, *ApJ*, **856**, 69
- Davies L. J. M., et al., 2016, *MNRAS*, **461**, 458
- Dekel A., Silk J., 1986, *ApJ*, **303**, 39
- Di Cintio A., Mostoghiu R., Knebe A., Navarro J. F., 2021, *MNRAS*, **506**, 531
- Doumler T., Hoffman Y., Courtois H., Gottlöber S., 2013, *MNRAS*, **430**, 888
- Driver S. P., et al., 2016, *MNRAS*, **455**, 3911
- Dutton A. A., et al., 2017, *MNRAS*, **467**, 4937
- Einasto J., Saar E., Kaasik A., Chernin A. D., 1974, *Nature*, **252**, 111
- Escala I., et al., 2018, *MNRAS*, **474**, 2194
- Fillingham S. P., Cooper M. C., Pace A. B., Boylan-Kolchin M., Bullock J. S., Garrison-Kimmel S., Wheeler C., 2016, *MNRAS*, **463**, 1916
- Ford G. P., et al., 2013, *ApJ*, **769**, 55
- Fossati M., et al., 2015, *MNRAS*, **446**, 2582
- Gallart C., et al., 2015, *ApJ*, **811**, L18
- Gallazzi A., Charlot S., Brinchmann J., White S. D. M., Tremonti C. A., 2005, *MNRAS*, **362**, 41
- Garrison-Kimmel S., et al., 2019, *MNRAS*, **489**, 4574
- Genina A., Frenk C. S., Benítez-Llambay A. r., Cole S., Navarro J. F., Oman K. A., Fattahi A., 2019, *MNRAS*, **488**, 2312
- Gottlöber S., Hoffman Y., Yepes G., 2010, arXiv e-prints, p. arXiv:1005.2687
- Grcevich J., Putman M. E., 2009, *ApJ*, **696**, 385
- Gunn J. E., Gott J. Richard I., 1972, *ApJ*, **176**, 1
- Hall C., Courteau S., Jarrett T., Cluver M., Meurer G., Carignan C., Audcent-Ross F., 2018, *ApJ*, **865**, 154
- Harris C. R., et al., 2020, *Nature*, **585**, 357
- Haynes M. P., et al., 2011, *AJ*, **142**, 170
- Hennebelle P., Chabrier G., 2013, *ApJ*, **770**, 150
- Hester J. A., 2006, *ApJ*, **647**, 910
- Hoffman Y., 2009, Gaussian Fields and Constrained Simulations of the Large-Scale Structure. pp 565–583, doi:10.1007/978-3-540-44767-2\_17
- Hoffman Y., Ribak E., 1991, *ApJ*, **380**, L5
- Hopkins P. F., et al., 2018, *MNRAS*, **480**, 800
- Hunter J. D., 2007, *Computing in Science Engineering*, **9**, 90
- Kauffmann G., et al., 2003, *MNRAS*, **341**, 54
- Kawata D., Mulchaey J. S., 2008, *ApJ*, **672**, L103
- Kawata D., Gibson B. K., Barnes D. J., Grand R. J. J., Rahimi A., 2014, *MNRAS*, **438**, 1208
- Kennicutt Robert C. J., 1998, *ApJ*, **498**, 541
- Kennicutt Robert C. J., et al., 2003, *PASP*, **115**, 928
- Kennicutt R. C., et al., 2011, *PASP*, **123**, 1347
- Kirby E. N., Cohen J. G., Guhathakurta P., Cheng L., Bullock J. S., Gallazzi A., 2013, *ApJ*, **779**, 102
- Kormendy J., Sanders D. B., 1992, *ApJ*, **390**, L53
- Kravtsov A. V., Vikhlinin A. A., Meshcheryakov A. V., 2018, *Astronomy Letters*, **44**, 8
- Leroy A. K., Walter F., Brinks E., Bigiel F., de Blok W. J. G., Madore B., Thornley M. D., 2008, *AJ*, **136**, 2782
- Libeskind N. I., et al., 2020, *MNRAS*, **498**, 2968
- Licquia T. C., Newman J. A., 2015, *ApJ*, **806**, 96
- Macciò A. V., Udrescu S. M., Dutton A. A., Obreja A., Wang L., Stinson G. R., Kang X., 2016, *MNRAS*, **463**, L69
- Macciò A. V., Frings J., Buck T., Penzo C., Dutton A. A., Blank M., Obreja A., 2017, *MNRAS*, **472**, 2356
- Macciò A. V., Frings J., Buck T., Dutton A. A., Blank M., Obreja A., Dixon K. L., 2019, *MNRAS*, **484**, 5400
- Mateo M. L., 1998, *ARA&A*, **36**, 435
- McConnachie A. W., 2012, *AJ*, **144**, 4

- McGaugh S. S., 2005, *ApJ*, **632**, 859
- McGaugh S. S., 2012, *AJ*, **143**, 40
- Moster B. P., Macciò A. V., Somerville R. S., 2014, *MNRAS*, **437**, 1027
- Munshi F., Brooks A. M., Applebaum E., Weisz D. R., Governato F., Quinn T. R., 2017, arXiv e-prints, p. [arXiv:1705.06286](https://arxiv.org/abs/1705.06286)
- Obreja A., Stinson G. S., Dutton A. A., Macciò A. V., Wang L., Kang X., 2016, *MNRAS*, **459**, 467
- Obreja A., et al., 2019, *MNRAS*, **487**, 4424
- Okamoto S., Arimoto N., Yamada Y., Onodera M., 2012, *ApJ*, **744**, 96
- Peebles M. S., Werk J. K., Tumlinson J., Oppenheimer B. D., Prochaska J. X., Katz N., Weinberg D. H., 2014, *ApJ*, **786**, 54
- Pilkington K., et al., 2012, *MNRAS*, **425**, 969
- Planck Collaboration et al., 2014, *A&A*, **571**, A16
- Pontzen A., Roškar R., Stinson G., Woods R., 2013, pynbody: N-Body/SPH analysis for python (ascl:1305.002)
- Putman M. E., Zheng Y., Price-Whelan A. M., Grcevich J., Johnson A. C., Tollerud E., Peek J. E. G., 2021, *ApJ*, **913**, 53
- Ritchie B. W., Thomas P. A., 2001, *MNRAS*, **323**, 743
- Saintonge A., et al., 2011, *MNRAS*, **415**, 32
- Sand D. J., Seth A., Olszewski E. W., Willman B., Zaritsky D., Kallivayalil N., 2010, *ApJ*, **718**, 530
- Sawala T., Scannapieco C., White S., 2012, *MNRAS*, **420**, 1714
- Shen S., Wadsley J., Stinson G., 2010, *MNRAS*, **407**, 1581
- Simon J. D., et al., 2021, *ApJ*, **908**, 18
- Skillman E. D., Kennicutt R. C., Hodge P. W., 1989, *ApJ*, **347**, 875
- Sofue Y., 2015, *PASJ*, **67**, 75
- Sorce J. G., 2015, *MNRAS*, **450**, 2644
- Sorce J. G., 2018, *MNRAS*, **478**, 5199
- Sorce J. G., Guo Q., 2016, *MNRAS*, **458**, 2667
- Sorce J. G., Courtois H. M., Gottlöber S., Hoffman Y., Tully R. B., 2014, *MNRAS*, **437**, 3586
- Sorce J. G., et al., 2016, *MNRAS*, **455**, 2078
- Spekkens K., Urbancic N., Mason B. S., Willman B., Aguirre J. E., 2014, *ApJ*, **795**, L5
- Stinson G., Seth A., Katz N., Wadsley J., Governato F., Quinn T., 2006, *MNRAS*, **373**, 1074
- Stinson G. S., Brook C., Macciò A. V., Wadsley J., Quinn T. R., Couchman H. M. P., 2013, *MNRAS*, **428**, 129
- Su K.-Y., Hopkins P. F., Hayward C. C., Faucher-Giguère C.-A., Kereš D., Ma X., Robles V. H., 2017, *MNRAS*, **471**, 144
- Thomas D., Maraston C., Bender R., Mendes de Oliveira C., 2005, *ApJ*, **621**, 673
- Tully R. B., et al., 2013, *AJ*, **146**, 86
- Virtanen P., et al., 2020, *Nature Methods*, **17**, 261
- Wadsley J. W., Veeravalli G., Couchman H. M. P., 2008, *MNRAS*, **387**, 427
- Wadsley J. W., Keller B. W., Quinn T. R., 2017, *MNRAS*, **471**, 2357
- Wang L., Dutton A. A., Stinson G. S., Macciò A. V., Penzo C., Kang X., Keller B. W., Wadsley J., 2015, *MNRAS*, **454**, 83
- Weisz D. R., Dolphin A. E., Skillman E. D., Holtzman J., Gilbert K. M., Dalcanton J. J., Williams B. F., 2014, *ApJ*, **789**, 148
- White S. D. M., Frenk C. S., 1991, *ApJ*, **379**, 52
- White S. D. M., Rees M. J., 1978, *MNRAS*, **183**, 341
- Williamson D., Martel H., Romeo A. B., 2016, *ApJ*, **831**, 1
- Wilman D. J., Zibetti S., Budavári T., 2010, *MNRAS*, **406**, 1701
- Yin J., Hou J. L., Prantzos N., Boissier S., Chang R. X., Shen S. Y., Zhang B., 2009, *A&A*, **505**, 497
- Zaroubi S., Hoffman Y., Fisher K. B., Lahav O., 1995, *ApJ*, **449**, 446

This paper has been typeset from a  $\text{\TeX}/\text{\LaTeX}$  file prepared by the author.